

Seismic tomography of the Gulf of Corinth: a comparison of methods

Helene Le Meur⁽¹⁾(*), Jean Virieux⁽²⁾ and Pascal Podvin⁽³⁾

⁽¹⁾ Département de Sismologie, IPGP, T14-24, Paris, France

⁽²⁾ Géosciences Azur, CNRS-UNSA, Valbonne, France

⁽³⁾ École des Mines de Paris, Fontainebleau, France

Abstract

At a local scale, travel-time tomography requires a simultaneous inversion of earthquake positions and velocity structure. We applied a joint iterative inversion scheme where medium parameters and hypocenter parameters were inverted simultaneously. At each step of the inversion, rays between hypocenters and stations were traced, new partial derivatives of travel-time were estimated and scaling between parameters was performed as well. The large sparse linear system modified by the scaling was solved by the LSQR method at each iteration. We compared performances of two different forward techniques. Our first approach was a fast ray tracing based on a paraxial method to solve the two-point boundary value problem. The rays connect sources and stations in a velocity structure described by a 3D B-spline interpolation over a regular grid. The second approach is the finite-difference solution of the eikonal equation with a 3D linear interpolation over a regular grid. The partial derivatives are estimated differently depending on the interpolation method. The reconstructed images are sensitive to the spatial variation of the partial derivatives shown by synthetic examples. We also found that a scaling between velocity and hypocenter parameters involved in the linear system to be solved is important in recovering accurate amplitudes of anomalies. This scaling was estimated to be five through synthetic examples with the real configuration of stations and sources. We also found it necessary to scale P and S velocities in order to recover better amplitudes of S velocity anomaly. The crustal velocity structure of a $50 \times 50 \times 20$ km domain near Patras in the Gulf of Corinth (Greece) was recovered using microearthquake data. These data were recorded during a field experiment in 1991 where a dense network of 60 digital stations was deployed. These microearthquakes were widely distributed under the Gulf of Corinth and enabled us to perform a reliable tomography of first arrival P and S travel-times. The obtained images of this seismically active zone show a south/north asymmetry in agreement with the tectonic context. The transition to high velocity lies between 6 km and 9 km indicating a very thin crust related to the active extension regime.

Key words seismic tomography – ray tracing – eikonal equation – inversion – Gulf of Corinth

1. Introduction

Seismic tomography has been proved to be an efficient tool to image the interior of the Earth. Since the well-known works of Aki and

Lee (1976) or Crosson (1976a,b) many authors have used first-arrival times to recover the 3D seismic velocity structure as well as hypocenter coordinates at local, regional and global scales.

The travel-time tomography approach is based on the following equation

$$T(x_s, x_r) = \int_{\mathcal{L}} u(x(\xi)) d\xi \quad (1.1)$$

giving the travel-time T between the source x_s and the station x_r where the slowness u is integrated along an extremal ray \mathcal{L} (often the fastest one) sampled by the variable ξ . Because the ray \mathcal{L} depends on the unknown seismic structure de-

(*) Now at: Dipartimento di Geofisica e Vulcanologia, Università di Napoli Federico II, Largo San Marcellino, 10, 80138 Napoli, Italy.

Mailing address: Dr. Helene Le Meur, Département de Sismologie, IPGP, T14-24, 4ème, 4 Place Jussieu, 75005 Paris, France; e-mail: helene.le.meur@geologie.ens-lyon.fr

scribed by the slowness u or any equivalent field, the inverse problem of finding the seismic structure from travel-times is truly non-linear.

This intrinsic non-linearity of travel-time tomography impels many authors to adopt an iterative linearized inversion scheme. At a given iteration n , the current travel-time $T_n(\mathbf{x}_s, \mathbf{x}_r)$ is estimated along a ray curve \mathcal{L}_n which is already defined at the previous iteration in the recovered slowness field $u_{n-1}(\mathbf{x})$. The perturbation in travel-time is given by the following equation

$$\delta T(\mathbf{x}_s, \mathbf{x}_r) = T_n - T_{n-1} = \int_{\mathcal{L}_n} \delta u(\mathbf{x}(\xi)) d\xi \quad (1.2)$$

where $T_{n-1}(\mathbf{x}_s, \mathbf{x}_r)$ is the travel-time at the previous iteration and $\delta u(\mathbf{x})$ is the expected perturbation in slowness at the current iteration. This linearized approach has been called delay time tomography by Nolet (1981). Let us emphasize that the ray curve \mathcal{L}_n is updated at each iteration in these approaches.

When the seismic sources are earthquakes, hypocenter parameters are unknown and also have to be determined at each iteration. We shall see that recovering velocity parameters and location as well as origin time parameters requires a normalization and a scaling between model parameters which modify the misfit function and the associated linear system to be solved.

We investigate two forward methods of travel-time computation and a single inversion technique. As will be shown, synthetic examples helped us assess the importance of different parameters such as discretization, normalization and interpolation. In order to show the applicability of our approach to real data, the assessment was done using the actual data acquisition geometry for a microearthquake experiment conducted around the Gulf of Corinth (Greece) in 1991. Finally, we present the results of this experiment.

2. Ray tracing approach versus wavefront approach

From reflection tomography (Farra *et al.*, 1989) and borehole tomography (Bregman

et al., 1989), the importance of accurate ray tracing has been emphasized. Because thousands of rays are traced at each iteration of the inversion, the ray tracing kernel of the seismic tomographic approach must be fast and robust. Disregarding approximate methods where rays are arbitrary curves (Thurber, 1983) or are traced in a one-dimensional medium (Al-Shukri and Mitchell, 1988), we have investigated two methods for performing 3D ray tracing.

In the first method, a path of extremal time (often the minimum time) is obtained between the source and the station by solving the ray tracing equations. This is the usual approach in seismology for many applications such as earthquake location and computation of seismograms. This approach is very efficient in layered media. In the case of a three-dimensional heterogeneous geometry, the difficult problem of connecting the source and the receiver by the ray with minimum travel-time has never been solved exactly (Sambridge and Kennett, 1986; Virieux *et al.*, 1988). We adopt a shooting method to reach the station based on a paraxial ray tracing as proposed by Virieux *et al.* (1988). For completeness, other methods exist to solve the two-point ray tracing problem, such as bending methods (Julian and Gubbins, 1977) or continuity methods (Keller and Perozzi, 1983) but they share the same drawback as the method we are using: they offer no guarantee that the global minimum travel-time ray is obtained.

Recently, several authors proposed another strategy based on wavefront construction which has its roots in the earlier work of Riznichenko (1946). The computer strategy was proposed by Vidale (1988) and improved subsequently by different authors. Among these works, a 3D extension of the work of Podvin and Lecomte (1991) will be used in our investigation. This method reconstructs wavefronts of equal travel-time through the entire 3D medium. It has the important advantage with respect to the previous method in that the selected ray between the source and the receiver is the global minimum travel-time ray. On the other hand, we must expect an increase in computer time for this approach because the

sampling of the entire medium is required for each source. Of course, one can interchange receivers and sources because we have fewer stations than earthquakes as proposed by Podvin and Lecomte (1991) among others. Hence, we only need one travel-time calculation per station at each iteration. Once these wavefronts have been constructed from a given receiver, a local evaluation of the time gradient perpendicular to the wavefront allows us to trace rays, starting from points in the medium (considered as sources) back to the receiver. We call this known method the wavefront approach.

3. Model description: slowness with linear interpolation versus squared slowness with B-spline interpolation

There are many possible descriptions of a velocity structure. Two quantities are often selected in seismic tomography as the parameter to invert. The first one is the velocity distribution because it is the natural quantity analyzed by seismologists. The second one is the slowness distribution because it appears as the simplest quantity in the linearized travel-time integral which connects the source and the receiver (as shown by (eq. 1.2)). Because the wavefront approach is based on locally straight rays, the slowness parameter is the natural parameter to describe the medium in that approach. The grid used for travel-time calculation is ten times finer than the grid for the inversion which provides a modelling error of travel-times lower than 5 ms in the synthetic examples of this paper.

In the case of the ray approach, the square of slowness is the preferred quantity to be inverted because it is connected directly to the ray tracing system. With that parameter selection, the corresponding ray equations

$$\begin{aligned}\frac{d\mathbf{x}}{d\tau} &= \mathbf{p} \\ \frac{d\mathbf{p}}{d\tau} &= \frac{1}{2} \nabla u^2 \\ \frac{dT}{d\tau} &= u^2,\end{aligned}\quad (3.1)$$

are actually very simple (Burridge, 1976; Farra and Madariaga, 1987). The position of the ray is denoted by \mathbf{x} and the slowness vector by \mathbf{p} . These quantities are sampled by a ray parameter $d\tau$ related to the arc length ds by $ds = u d\tau$. Tracing rays consists of solving the first two equations while calculating the travel-time T is an integration of the squared slowness along the ray as shown by the third equation. Our strategy to reach the station using paraxial ray tracing requires continuous, smoothly interpolated values of the squared slowness as well as its first-order spatial derivatives. We chose a B-spline interpolation of order 4 for the square of the slowness between nodes of the inversion grid. The sampling $d\tau$ along the ray is taken to be such that the associated arc length is around one tenth of the grid spacing. With that fine sampling along the ray, travel-times are computed with a precision lower than 2 ms for the presented synthetic examples.

We shall consider these two methods for estimating travel-times between sources and receivers. In both cases, the parameter description is based on a continuous spatial function. We designed a computer code in which we could switch very easily from one forward method to the other when we found it more convenient.

4. Linearized approach of travel-time inversion

Once an initial medium has been defined, travel-times at each station for each earthquake can be estimated. Partial derivatives of travel-time with respect to values on nodes of the inversion grid are computed either with linearly interpolated slowness or with B-spline interpolation for the squared slowness. Because rays are lines in a three-dimensional medium, for a given pair of source and receiver, only nearby nodes have non-zero partial derivatives for seismic structure inversion. Consequently, the associated inverse linear system is sparse. More precisely, each portion of a ray inside a cell contributes to the partial derivatives of 8 nodes for the wavefront approach and of 64 nodes for the ray approach. The sparsity of the

linear system of the travel-time tomography is less important for the ray approach than for the wavefront approach, but it is still present.

Partial derivatives for hypocenter positions and origin time are also computed and increase dramatically the size of the linear system to be solved. The linear system has a specific structure related to the difference between medium parameters and hypocenter parameters. Because an individual earthquake is independent of all the others, the matrix of partial derivatives with respect to hypocenter parameters contains zero values for all elements except the four corresponding to that particular hypocenter.

For solving such large sparse linear systems, two methods are prevalent in seismic tomography: the SIRT method and the LSQR method (van der Sluis and van de Vorst, 1987). The SIRT method (Dines and Lytle, 1979; Ivansson, 1983) does not converge to the least squares solution. We prefer the LSQR method of Paige and Saunders (1982) which is based on the conjugate gradient approach. It is superior both in terms of fast convergence rate (Nolet, 1985) and reduced propagation of data errors. A recent extension of the SIRT method, DSIRT (Trampert and Léveque, 1990), reduces the bias of the SIRT method but does not exhibit any interesting new feature to prefer it to the LSQR method. The LSQR method is becoming increasingly the method of choice in seismic tomographic problems (Spakman and Nolet, 1988; Bregman *et al.*, 1989) and we also selected it in our approach.

5. Inversion scheme: scaling operation and *a priori* information

Before solving the linearized system

$$\mathcal{A} dm = dt, \quad (5.1)$$

where \mathcal{A} is the matrix of partial derivatives, dm are perturbations of model parameters and dt are time delays observed at stations, one must take into consideration the units used for the different parameter quantities. The misfit

function S for a given model dm in the data space

$$S(dm) = \sum_{i=1}^N (T_{\text{obs}}^i - T_{\text{synt}}^i(dm))^2 \quad (5.2)$$

has a shape depending on parameter values. The indice i denotes travel-time data. The P -wave velocity has the same units as the S -wave velocity while hypocenter parameters (source coordinates and origin time) have quite different units. Changing units will modify the shape of the misfit function as noted by Nolet (1987) towards a more or less spherical shape adapted for downhill investigation. If we change units, we also modify partial derivatives in order to preserve the linear system (5.1). Equivalently, one can modify partial derivatives and deduce the associated units.

We propose the following strategy of changing units of each class of parameters which are P velocity, S velocity, hypocenter locations and hypocenter origin time through normalization of partial derivatives. We estimate the norm of each column of the matrix \mathcal{A} corresponding to one parameter and the maximum norm for each class of parameters. We normalize with the help of the maximum norm the columns of the matrix \mathcal{A} associated with a given class of parameters to a given specified weight for this class. The units of the class of parameters are modified accordingly to preserve the system (5.1).

The definition of the weighting which makes one class of parameters more or less sensitive to the data is performed through synthetic examples for the real configuration of stations and seismic sources. We found that the different weights depend on the geometry of each experiment.

This strategy is called the scaling operation and, although this transformation is performed on model parameters, it modifies the linear system (5.1) and, consequently, the shape of the misfit function defined the data space. This scaling procedure is one way to amplify the effect of the data space on a given set of model parameters to be determined. Spakman (1988) also performed a quantitative numerical analysis of such influence and proposed data covari-

ance matrices for recovering both P and S velocities. These covariance matrices also modify the shape of the misfit function in a slightly different way, making a correspondence between the scaling operation and the data covariance definition difficult. We selected the scaling operation as a preconditioning operation for recovering different sets of parameters.

The solution of this scaled linearized problem was then obtained by iterative damped least squares by extending the misfit function

$$S'(dm) = \sum_{i=1}^N (T_{\text{obs}}^i - T_{\text{synt}}^i(dm))^2 + \alpha dm^2 \quad (5.3)$$

with *a priori* information in the model space. Travel-time tomography is almost always an ill-posed problem which is both overdetermined and underdetermined (Menke, 1984). Therefore, it requires regularization or some type of model norm constraint to avoid dramatic effects associated with small singular values of the linear system. This regularization can be introduced either by the choice of a damping factor α or by the use of covariance matrix on model parameters (Tarantola and Valette, 1982). We chose to introduce a damping factor α , and determined it through synthetic examples.

Finally, additional weightings based on the quality of the reading, on the size of residuals and on the source-receiver distance are applied throughout the inversion. In our applications, we consider four kinds of reading. We take out data leading to time residuals over 2 s and we assign a reducing weight to the data associated with a ray over 100 km long. This weight goes to zero for a ray over 200 km long.

The non-linearity associated with the updating of rays at each iteration makes the estimation of resolution more difficult. Again, we believe that resolution estimation is still possible through synthetic examples where one tries to recover a local anomaly with the real acquisition geometry of a tomographic experiment. This is not performed in this paper devoted to the investigation of the influence of the forward modeling in the inversion results.

6. Synthetic examples

6.1. Recovering a simple velocity anomaly

We start with a simple case where sources are evenly distributed at a depth of 20 km and stations are irregularly distributed at the free surface above a positive anomaly of P -wave velocity. Synthetic travel-time data set is obtained through the ray approach or the wavefront approach with a discretization so fine that the difference in travel-time is lower than 1 ms. We shall invert for the P -wave velocity starting with an initial medium without this anomaly.

In this first example, the 3D model is discretized on a grid of 10 by 10 by 6 nodes. The node spacing is 6 km in all directions. In this example as well as the following ones, 3D velocity models are represented with a series of horizontal slices sorted by increasing depth (here every 3 km). The original P -wave velocity model with the synthetic positive anomaly is displayed in fig. 1a from the surface down to 18 km depth. Figure 1b shows the P -wave velocity model solution using the ray tracing method. The anomaly is correctly located and its amplitude is almost exactly recovered. We emphasize that the squared slowness is actually the inverted parameter even though we display the associated velocity structure. Figure 1c shows the P -wave velocity model reconstructed using the wavefront approach where slowness is the selected parameter for describing the medium. We find that the shape of the anomaly is correctly recovered but the amplitude is less accurate than in the previous case.

The evolution of the global misfit function (fig. 2) shows the rapid convergence for this relatively simple geometry: the convergence of the misfit function is reached after three iterations when the forward problem is solved by the ray tracing. The convergence is slower with the wavefront approach and the value of the misfit function is higher than that obtained with the ray approach. We believe that the better performance of the ray method compared to the wavefront approach comes from its smoother interpolation.

This simple example allows us to validate the ability of the LSQR algorithm to recover a P -wave velocity anomaly with two different

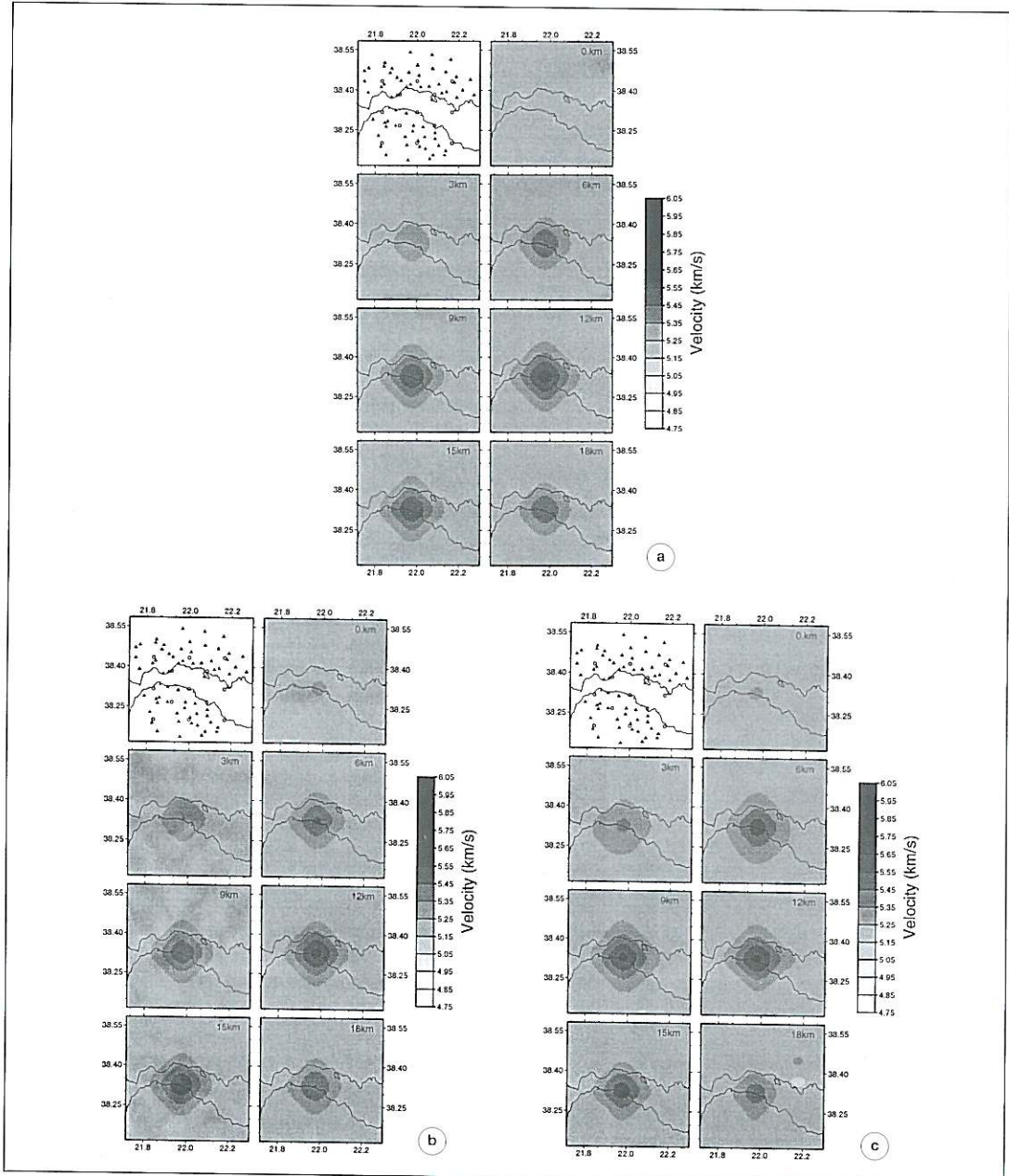


Fig. 1a-c. A synthetic test for recovering a high velocity anomaly using real station distribution and hypothetical well distributed hypocenters: the positive anomaly is centered at 12 km depth and reaches a value of 5.6 km/s embedded in a homogeneous velocity of 5.2 km/s. a) The 3D P velocity model to be recovered. b) Reconstructed 3D P velocity model using the ray tracing method. c) Reconstructed 3D P velocity model using the wavefront method.

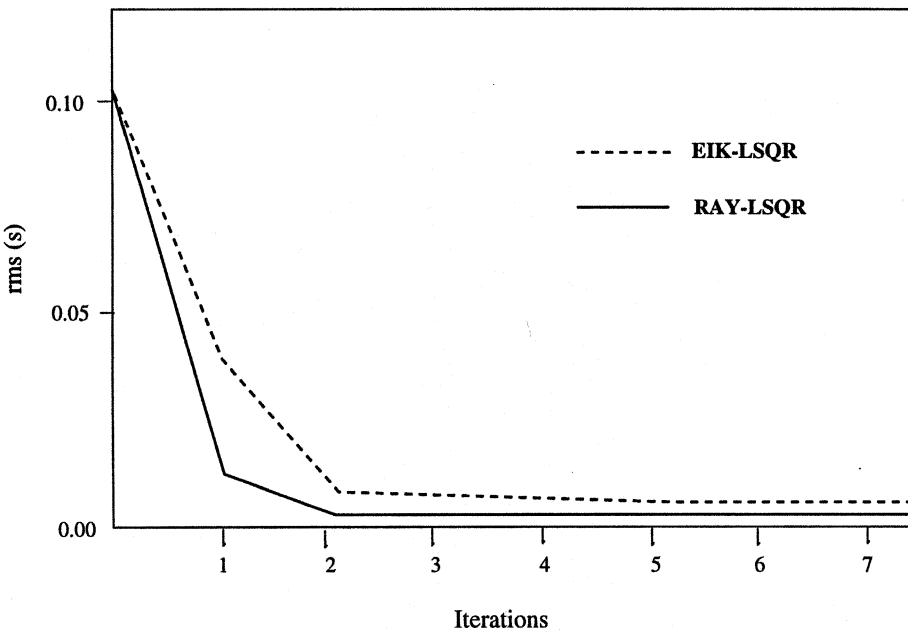


Fig. 2. The minimum of the global misfit function is reached after 3 iterations. We might notice that the convergence is faster for the ray approach than for the wavefront approach.

forward methods where both the inverted medium parameter and the interpolation on the discrete grid are different.

6.2. Checker-board test

After this simple case, we carried out a checker-board sensitivity test. Despite the limitations of this test (Lévéque *et al.*, 1993), it provides useful hints about the spatial resolution associated mainly with the ray coverage.

We specified values of the velocity as a sinusoidal function with a wavelength (18 km) larger than the distance between nodes (6 km) with a 5% undulation with respect to a homogeneous medium. For the wavefront approach, we considered the same values but the interpolation was linear. We present a comparison of the recovered velocity structure using the two different forward methods combined with the inverse LSQR method. Figure 3a displays the original velocity model and fig. 3b,c shows the

velocity structures obtained after five iterations starting from a homogeneous initial velocity model in both cases. The velocity structure is well recovered using the ray approach but B-spline interpolation smears out from surrounding layers small artifacts at depths where we expect a homogeneous value. The velocity structure is less reconstructed with the wavefront approach because the spatial frequency content is higher for the linear interpolation.

This test demonstrates the effects of parameterization and interpolation used by the two forward methods which produce significantly different results. With the same grid node spacing, we expect smoother images for the ray approach compared to those obtained with the wavefront approach.

6.3. Influence of scaling operation

Let us consider now the more realistic case in which all parameters are involved. We found

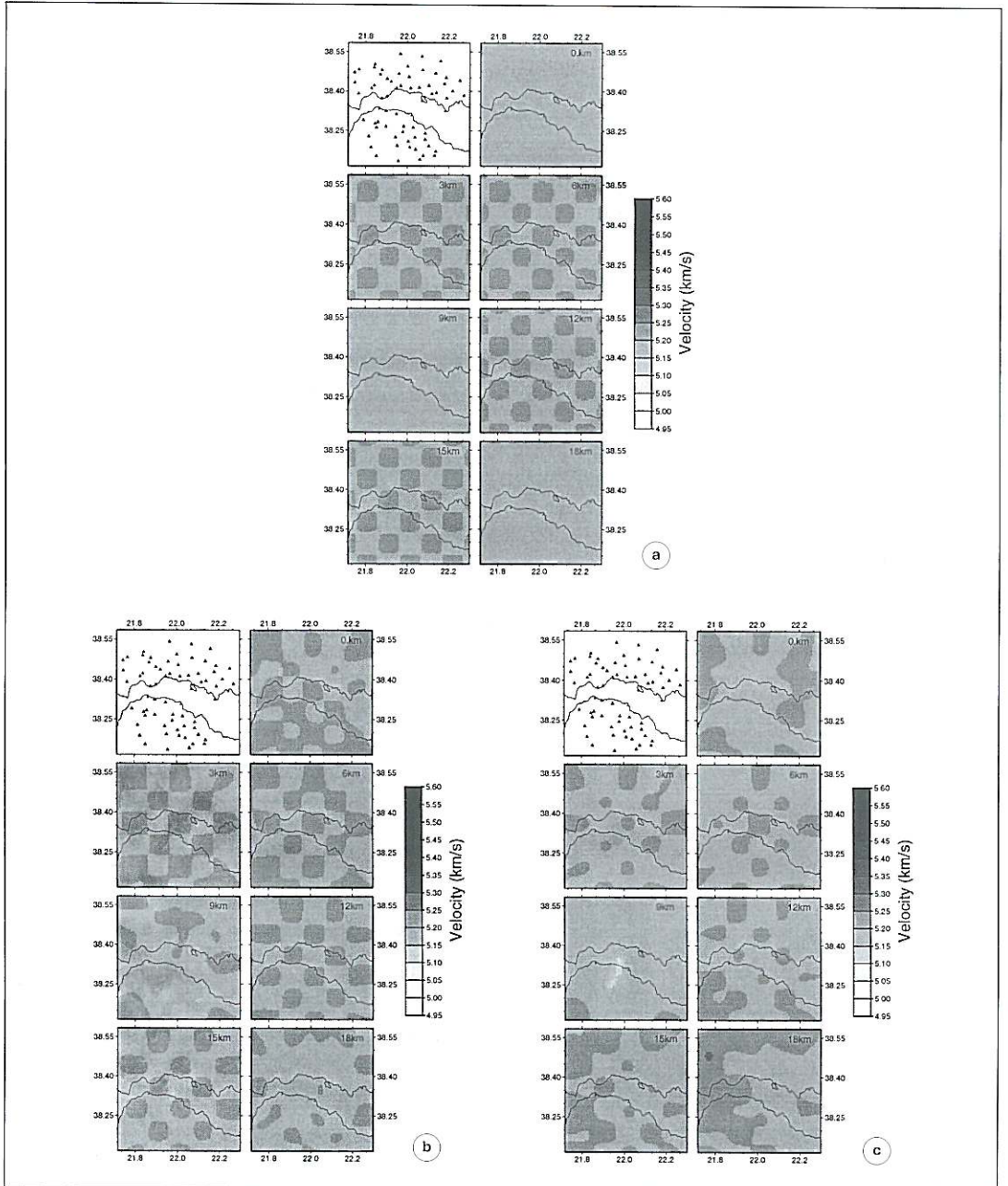


Fig. 3a-c. Comparison between the two proposed forward methods: a positive and negative pattern is recovered from an initial model with uniform velocity. a) The 3D P velocity model to be recovered. b) The recovered 3D P -wave velocity model using both ray tracing and LSQR. c) The recovered 3D P -wave velocity model using both wavefront tracing and LSQR.

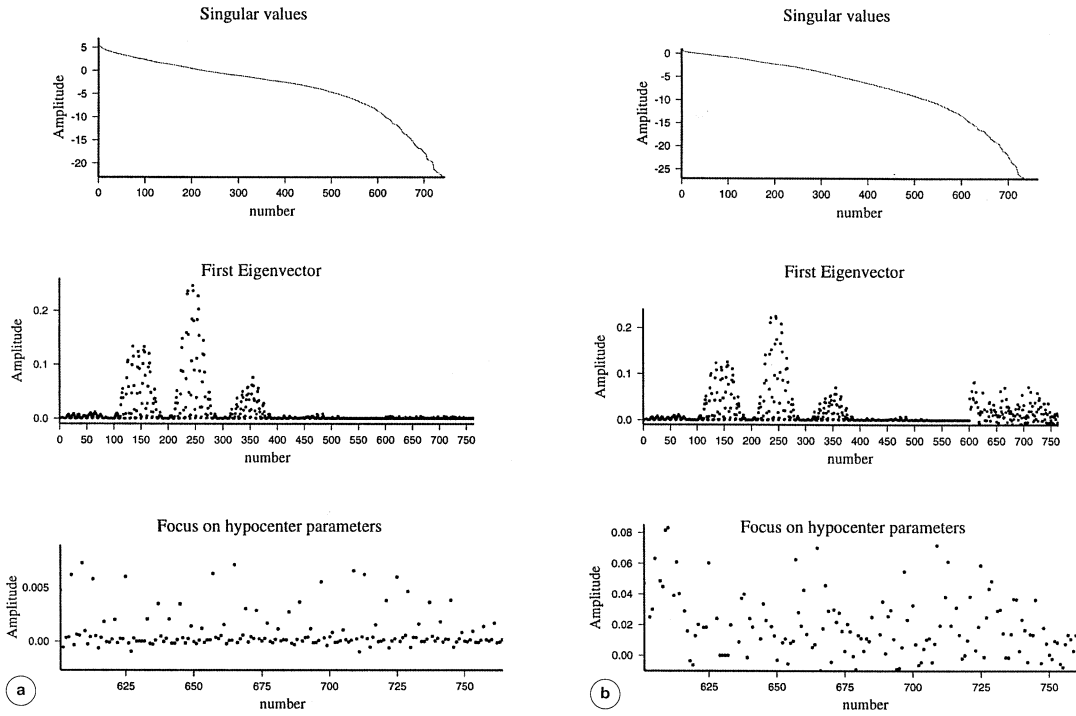


Fig. 4a,b. Quantification of the scaling between parameters. First eigenvector composition before (a) and after (b) rescaling entire system. Note the relatively unchange shapes of the singular values and the strong amplification of the hypocenter parameters compared with the 600 velocity parameters. The zoom performed on hypocenter parameters shows also a partition on the left between origin time parameter and location parameters for hypocenters while on the right this pattern tends to disappear.

that scaling is important between hypocenter parameters and velocity parameters but also between P and S velocity parameters. A quantitative analysis using the Singular Value Decomposition (SVD approach) illustrates this point. For these tests, we kept the same receiver distribution as the previous example. The velocity medium is sampled with the same discretization (grid spacing of 6 km leading to 600 velocity parameters and 58 sources evenly distributed at 20 km depth).

With this geometry, the SVD analysis shows the following features of the linear system: on the top panel, fig. 4a displays the singular values in a decreasing order on a logarithmic scale showing that the tomographic problem is extremely ill-conditioned. The cen-

tral panel exhibits components of the first eigenvectors (corresponding to the highest eigenvalue). The 600 first components are associated with the velocity parameters while the 58×4 last ones correspond to hypocenter parameters. Velocity parameters associated with the highest values correspond to those well-sampled by rays under the network center. In comparison, components associated with the hypocenter parameters are all very small. If we zoom this last group of parameters in the bottom panel, components representing origin times have higher values than those associated with hypocenter positions. This quantitative analysis of eigenvector amplitude is a demonstration of the need for normalization of model parameters. This is why we adopted a normal-

ization scheme and a scaling operation as explained earlier to rescale the entire system. Figure 4b presents the same results as fig. 4a but for the normalized system. Note the expected effects in the second and third panels where the values of the different components reach an equivalent level.

The need for a normalization between the P and S velocity parameters is illustrated in the spherical anomaly test where both P and S velocity anomalies were sought. Although these quantities have the same physical dimension, the ratio between them effectively produces underweighting of S perturbations whereas P perturbations are effectively given a larger weight.

Figure 5a,b displays the P and S velocity structure to be recovered. The P and S solu-

tions are presented in fig. 6a,b. In these results, the amplitude of the S velocity anomaly was not recovered as accurately as the P velocity anomaly. When we introduced a relative weight for S velocity parameters as for the other classes of parameters, the results improved and the P and S velocity structures obtained using this weighting are displayed in fig. 7a,b.

It is interesting to note that a weighting ratio close to 2 between P and S velocity parameters had to be introduced in order to recover the correct amplitude of S -wave anomalies. In other words, we have made our data set twice as sensitive to S velocity variations. This feature may be related to the rather constant ratio between P and S velocities in the synthetic models around 1.80.

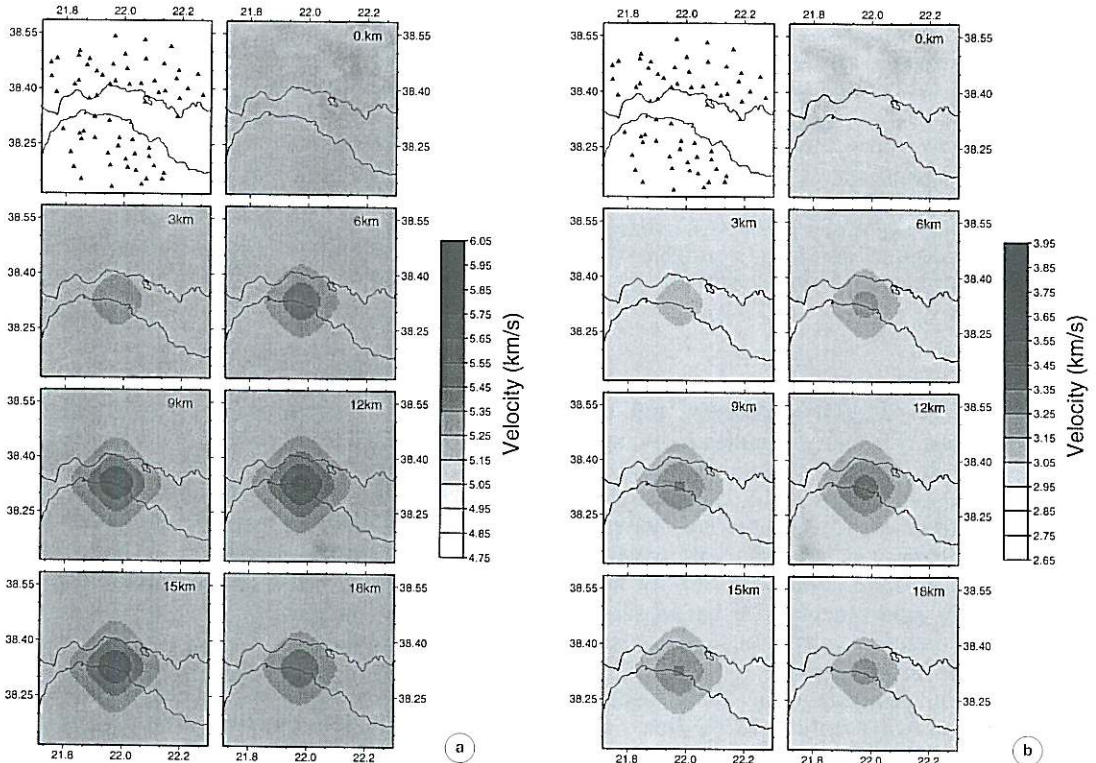


Fig. 5a,b. The 3D P (a) and S (b) velocity model to be recovered: see figs. 6a,b and 7a,b. The station distribution is shown on the left top panel while the source distribution is shown in figs. 6a,b and 7a,b.

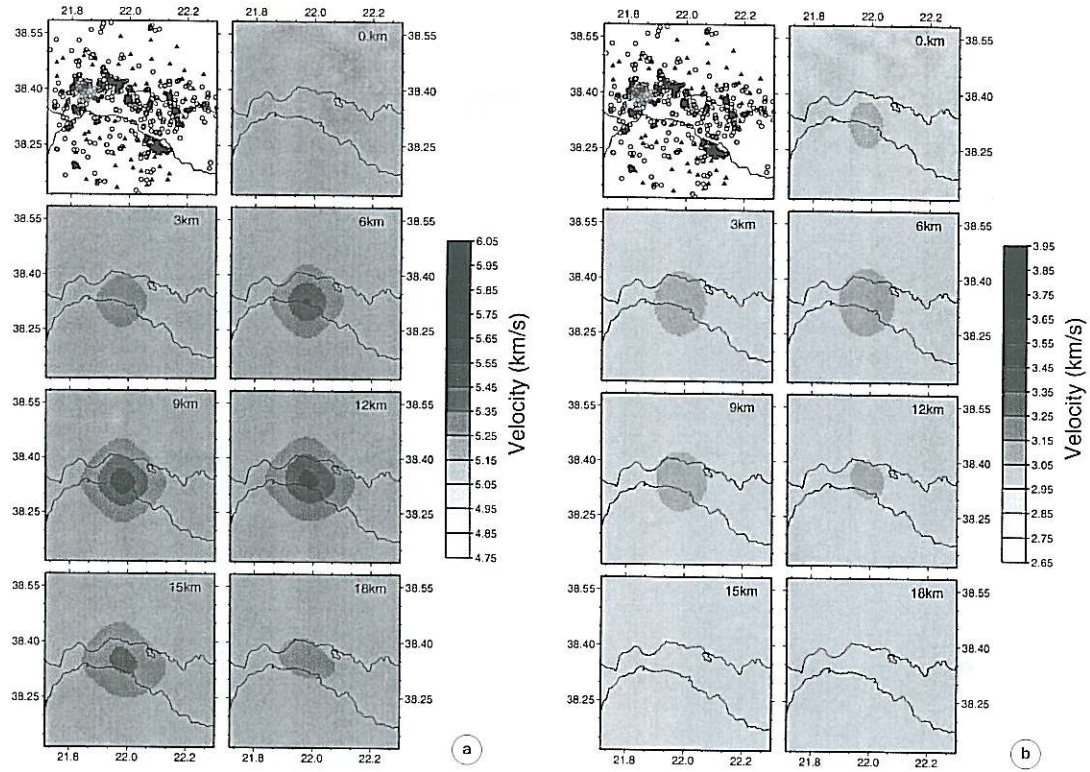


Fig. 6a,b. The 3D P (a) and S (b) wave velocity reconstructed models without scaling between P and S velocity parameters. Note the amplitude of the S velocity field is too small (fig. 6b). The real distribution of sources has been used in this simulation.

7. Application to the Gulf of Corinth

7.1. The Patras experiment of August 1991

We applied our inversion schemes to image the P -wave and S -wave velocity structure of a 50 km by 50 km by 20 km domain in the region of Patras (Gulf of Corinth in Greece), using microearthquake arrival times (fig. 8a,b). This data set of P and S phases was recorded during a twin French and Greek experiment conducted in July and August 1991. The general aim was the study of intracontinental crustal extension phenomena from tectonic, geodetic and seismological observations. The Gulf of Corinth was chosen because of its particularly interesting geodynamic situation: it

belongs to the Aegean domain, bounded by the North Anatolian Fault (NAF) and the Aegean arc, where the convergence of the African (South), Eurasian (North) and Arabian (East) plates takes place. Within these boundaries exists a N-S extensional regime responsible for one of the most seismically active zones in Europe. In addition to a significant number of large events (magnitude M_s 6.7 in 1861, M_s 6.7, 6.4, 6.4 in 1981, M_s 5.9 in 1992, M_s 6.2 in 1995), a relatively constant rate of moderate earthquakes is observed (M_s 5.5–6 every 4 or 5 years and ten times more events of M_s 4.5–5).

In this complex tectonic system, the most recent extensional structures are found in the Gulf of Corinth. A half-graben has been formed by the major active normal faults,

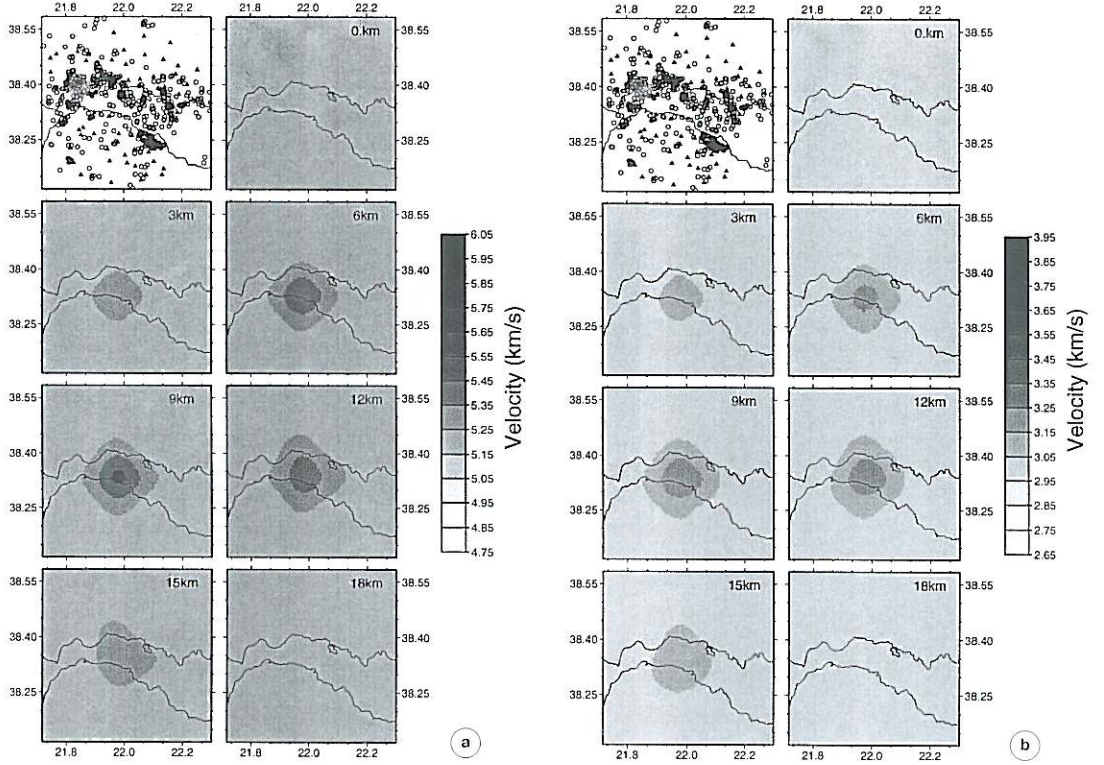


Fig. 7a,b. The 3D P (a) and S (b) wave velocity reconstructed models with scaling between P and S velocity parameters. Note the more accurate amplitude of the S velocity field (fig. 6b). The real distribution of sources has been used and allows us to use the selected scaling for the real data set.

which dip to the North with a characteristic length of 20–25 km and which are located on the southern coast (fig. 8a). The extension rate estimated in the gulf from GPS observations is 1.5 cm per year in a N10°E direction (Briole *et al.*, 1994) in agreement with the tectonic evidence of the extensional regime. A previous estimate for Central Greece from geodetical data collected over 100 years (Billiris *et al.*, 1991) yielded an extension rate of 1 cm per year.

Regarding the seismological part of the project, particular attention was paid to precise microearthquake locations and reliable focal mechanism solutions in order to constrain the fault distribution in depth and the deformation pattern in the seismic zone. Therefore, during

these two months, a dense network of 60 digital stations including 35 three-component stations (fig. 8b) was deployed on both sides of the gulf, within a 50 km by 50 km area. More than 5000 earthquakes were recorded in this period. The density of the network provides a good distribution of ray paths for hypocenter studies and tomographic inversions, although receivers in the gulf itself would have greatly improved the acquisition geometry.

Figure 8b shows that the hypocenter distribution is non-uniform: microevents are located in clusters as in any seismically active zone. Thus, initial hypocenter locations were found using the computer program HYPO71 (Lee and Lahr, 1975) in a 1D velocity model (Rigo, 1994).

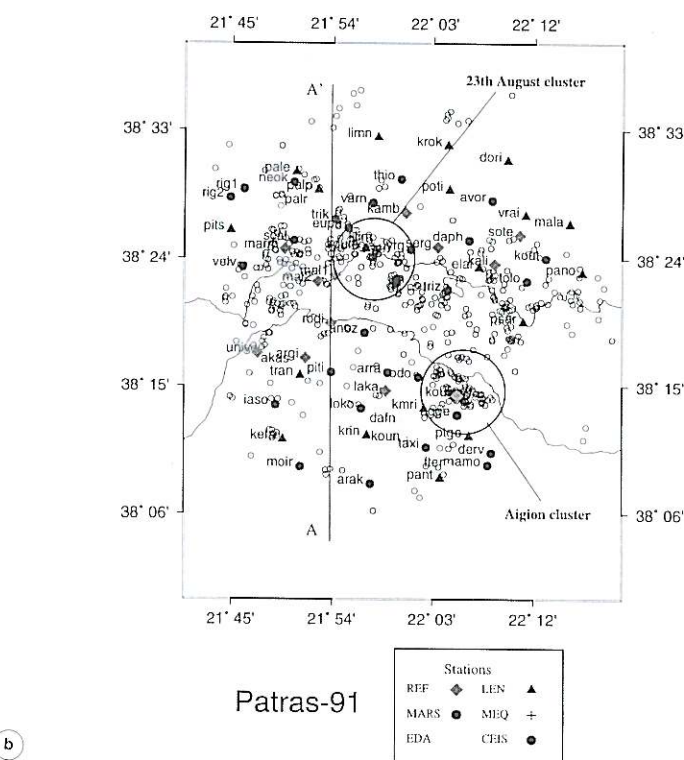
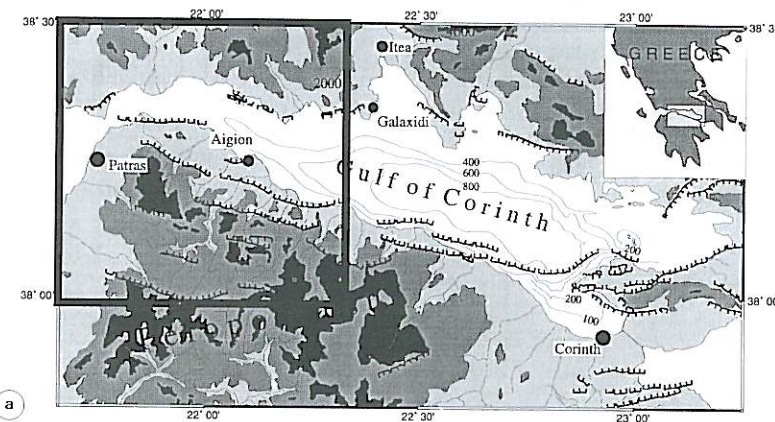


Fig. 8a,b. a) Schematic tectonic map of the Corinth Gulf: the tomographic area is displayed in the left box (Patras area). b) Patras area where more than 60 stations were deployed during summer 1991. Seismic network with different types of stations is shown as well as the selected microevents (circles). The distance between stations was less than 4 km. The seismic events selected for the tomography analysis are also shown.

Our main aim in this work is the determination of the seismic velocity structure of the asymmetric graben. We present geometrical information provided by our velocity model on the transition between superficial active structures of the graben and deeper tectonic structures.

7.2. Data selection and data analysis

The clustered distribution of sources is not optimal for our tomographic approach. In order to obtain a more homogeneous coverage, we selected data using different criteria for cluster events and for background seismicity. For clus-

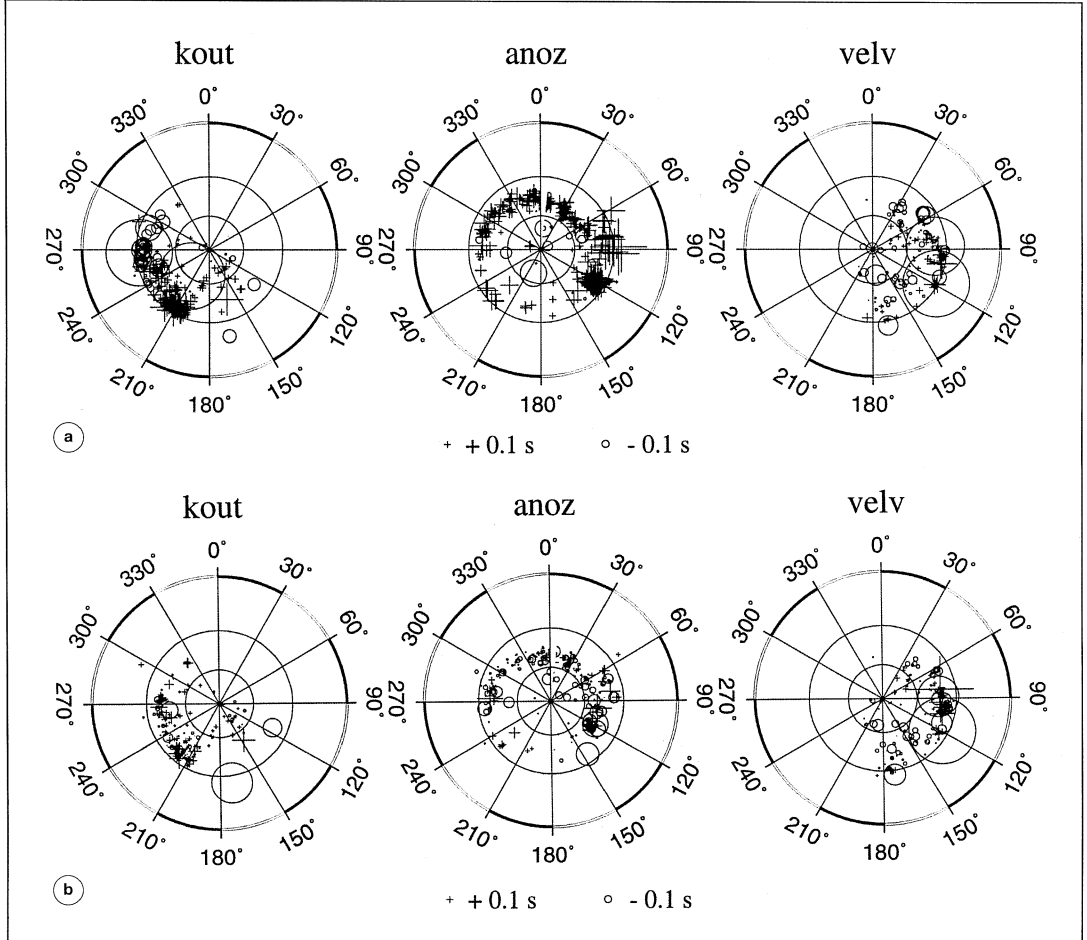


Fig. 9a,b. The local travel-time residual function are displayed in a stereographic projection for each station. This projection on a lower hemisphere is centered at the given station and uses angles obtained by the ray tracing. The amplitude of positive residuals (crosses) and negative residuals (circles) is proportional to the size of symbols. Three stations characteristic of different parts of the seismic network are shown: KOUT for the north-eastern part of the network, ANOZ for the central-southern and VELV for the western limit. a) Residuals obtained in the initial model (table I), before tomographic inversion; b) residual obtained after the tomographic inversion.

ters, we selected events recorded with more than nine high-quality P phases and with a r.m.s. travel-time residual lower than 0.15 s. Outside the clusters, we selected events with a minimum of five high-quality P arrivals with a r.m.s. value lower than 0.35 s. The resulting dataset consists of 641 microevents with 8301 picked P and 5638 S phases. The majority of these microevents lies between 6 km and 12 km depth and allows us to reliably image the structure down to this last depth.

The high quality of the recorded signals allowed accurate picking of the arrival times: the P phases were picked with an accuracy estimated to be 0.01 s for the three-component stations and 0.06 s for the one-component stations. The S phases are only picked on three-component stations with a lower accuracy of 0.1 s.

The initial analysis of travel-time residuals obtained with the 1D locations gave us a preliminary idea of the tomographic information that could be retrieved. The distribution of residuals at each station showed a coherent pattern either positive or negative with respect to emergent and azimuthal angles. Consequently, the tomographic inversion would convert these patterns into velocity anomalies. For each station, a stereographic projection on the lower hemisphere was performed using angles obtained by ray tracing. Figure 9a displays diagrams corresponding to three stations characteristic of different areas of the seismic network. On each diagram, the amplitude of positive residuals (crosses) and negative residuals (circles) is proportional to the size of symbols.

The first station KOUT displays a pattern of residuals characteristic of the north-eastern part of the network. These stations primarily recorded microevents of both the west and south-west clusters (see fig. 8b). The corresponding residuals present a pattern of negative and positive anomalies in azimuths from 240° to 270° induced by a 23rd August cluster and a pattern of positive anomalies in azimuths between 210° and 220° induced by the so-called Aigion cluster. The second station ANOZ is located in the central southern part of the gulf. The residuals are positive with notice-

ably large residuals from the Aigion cluster. The third station VELV, located at the north-western limit of the network, displays a pattern of residuals less easy to interpret.

From this residual data analysis, we found that there is one group of stations which recorded information with rather long ray paths sampling many different parts of the velocity structure. That shows clear evidence of lateral variation. There is a second group of stations that contain more local information which is less dependent on the ray azimuth and might thus be related to the structure near the receiver.

7.3. Resolution estimation

In order to estimate the effects of the uneven sampling of the region provided by the real distribution of the 641 hypocenters, we performed a checker-board test with the same velocity distribution as the one for the synthetic distribution of shots (see fig. 3a). We considered fixed earthquake hypocenters and inverted only for the velocity structure (see fig. 10): the well-resolved zones are beneath the center of the seismic network between the depths of 3 km and 9 km. We found that below 12 km the resolution is very poor because the velocity structure is sampled by only a few sources. The image shows that the poorly-resolved anomalies below 12 km are smeared up as high as 9 km depth. Therefore, although we present results down to the depth of 12 km, we shall have confidence only on anomalies above the depth of 9 km.

7.4. Initial models

The initial model has a strong influence in linearized tomographic inversion (Kissling *et al.*, 1994). Because we started with previously located hypocenters, we already partly defined our initial model. The previous knowledge of the seismic velocity is quite limited at this local scale (a 50 km by 50 km by 15 km box). We started with the 1D velocity model used by Rigo (1994) for hypocenter locations

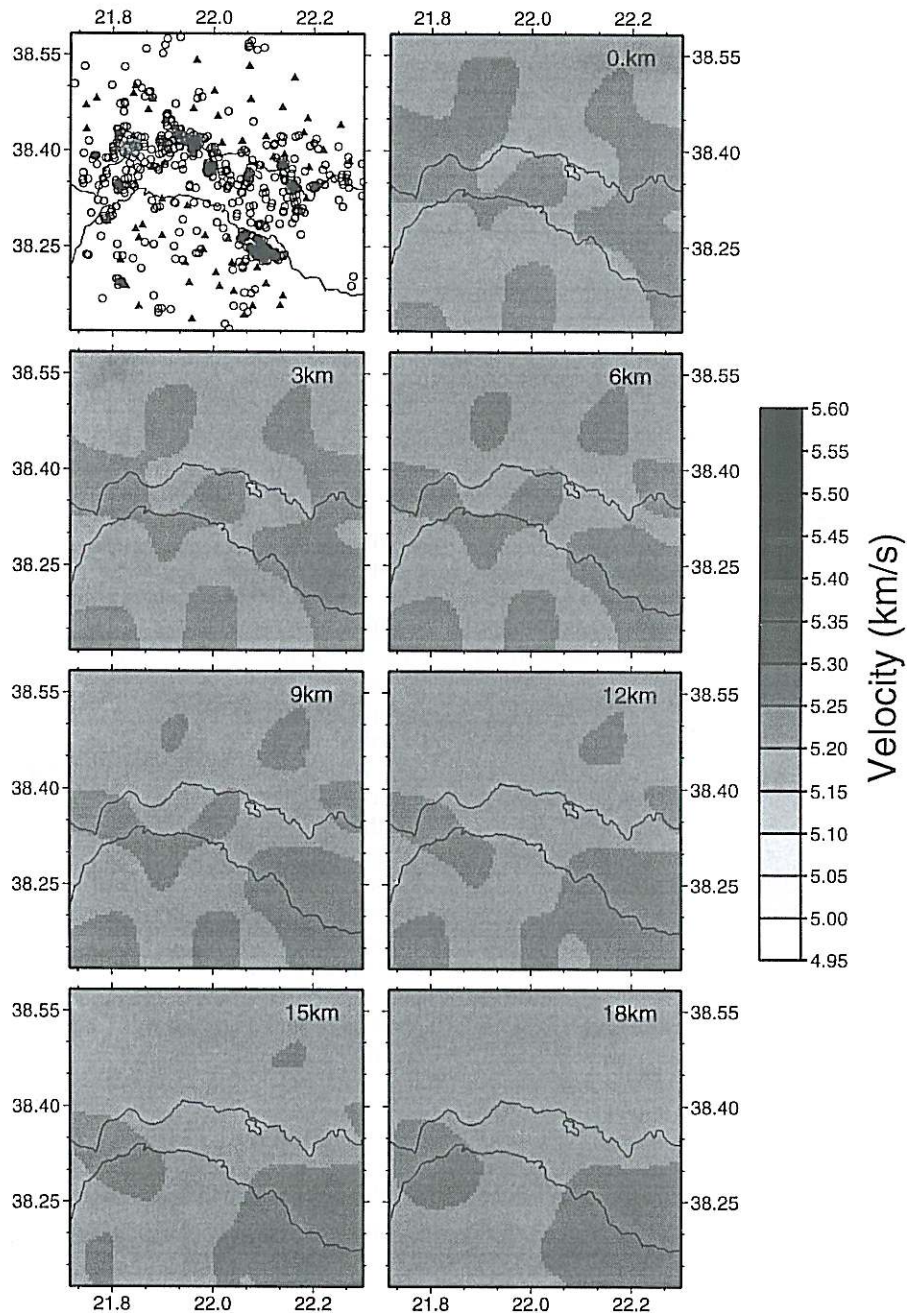


Fig. 10. The influence of the real hypocenter distribution on the resolved image: the zones of best resolution are located between 3 and 9 km depth under the center of the network area. Below 12 km depth, because of the lack of events, the velocity field is not resolved.

and we performed an inversion with fixed sources. We chose the average velocity for each layer in the resulting model as our initial 1D model. The discretization we considered has a 6 km grid step in each direction. We found that thus deduced 1D initial models (table I) give a lower global value of residuals than the Rigo 1D model.

The following inversion results were obtained starting from this initial P -wave velocity model and the S -wave velocity model corresponding to a constant V_p/V_s ratio of 1.80 (Rigo, 1994).

The P and S velocity models after six iterations of the linearized ray tracing inversion are displayed in fig. 11a,b. The optimal damping value 0.2 was obtained by trial and error and the relative weight between P and S velocities was close to 2 while the relative weight between P velocity and hypocenter parameters was around 5. The color scale indicates absolute values of velocity from the lowest value in red to the highest value in blue. This 3D velocity field is characterized by a large zone of low velocity in the southern part of the network and in the gulf, from the surface down to a depth of 3 km. At 3 km, this low velocity zone follows the shape of the sediment filled graben. Between 3 and 6 km depths, there is a sharp vertical increase in velocity. The structure of the graben is less pronounced and a high velocity structure appears just north of the gulf. This high anomaly increases in amplitude and extends further to the South with increasing depth. This anomaly extends at least to 12 km and might be related to tectonic structures older than the present extensional regime.

The variations observed in S velocity are similar to the P velocity anomalies in the upper 6 km where the V_p/V_s ratio is around 1.8. Using this S -wave velocity solution and the final hypocenter solutions, we computed synthetic travel-times and inverted starting from the 1D initial model following the procedure proposed by Zhao *et al.* (1992). We found that the recovered S velocity structure has a different pattern below 9 km depth. We conclude that the S velocity is not well constrained below 9 km and is stable only above that depth.

Table I. 1D P -wave velocity reference model for a vertical discretization step of 6 km.

Depth (km)	P velocity (km/s)
0	4.8
6	5.7
12	6.0
18	6.2
24	6.5

Because we inverted simultaneously for velocity structures and hypocenters, we found shifts in the microearthquake hypocenters which are displayed in fig. 12. In the bottom panel, crosses represent earthquake epicenters obtained after six iterations while empty circles symbolize the HYPO71 initial positions. A south-north vertical section shows the migration in depth of the hypocenters in the top panel. The most obvious feature is the spatial concentration of events inside clusters while events outside the network are moving away. In depth, the microevents are relocated deeper because the 3D velocity structure is faster on average than the 1D velocity structure. The relocation in the 3D heterogeneous velocity medium yields reduced travel-time residuals and provides a more reliable earthquake distribution.

7.5. Local misfit function

The global misfit function (fig. 13) shows a 25% reduction of the travel-time residuals during the iterative procedure from a r.m.s. value of 0.146 s down to 0.109 s. This global level remains above the expected accuracy of the travel-time picking. We believe that our forward modeling is unable to accurately synthesize travel-time residuals at some stations where fine scale structure very close to the station is important. An analysis of the local misfit function at each station will illustrate this feature.

For some stations, the local misfit function of travel-time residuals decreased by more than 75% while, for other stations, the local misfit

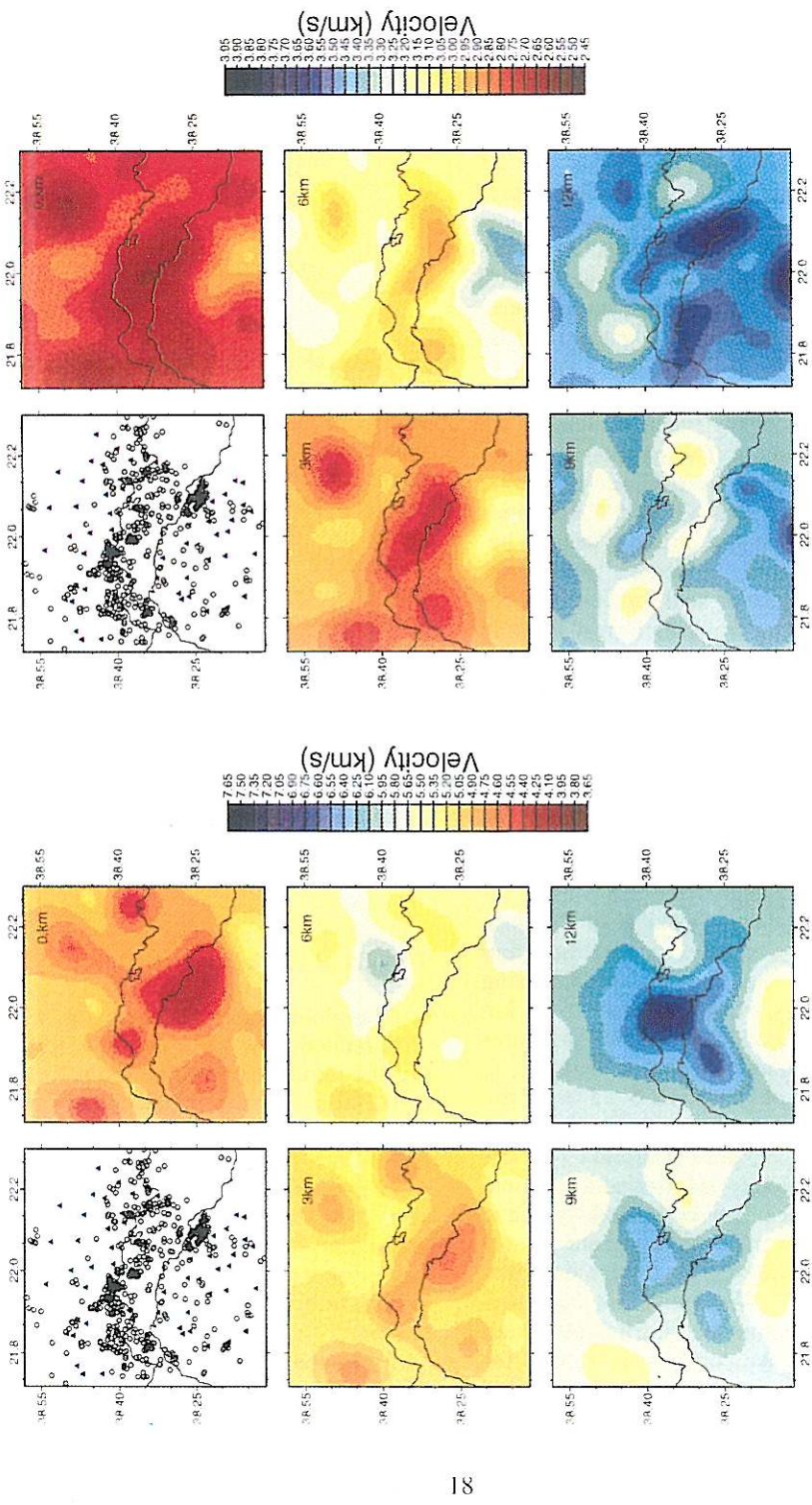


Fig. 11a,b. The 3D P (a) and S (b) velocity models after the joint inversion using ray tracing for a 6 km grid.

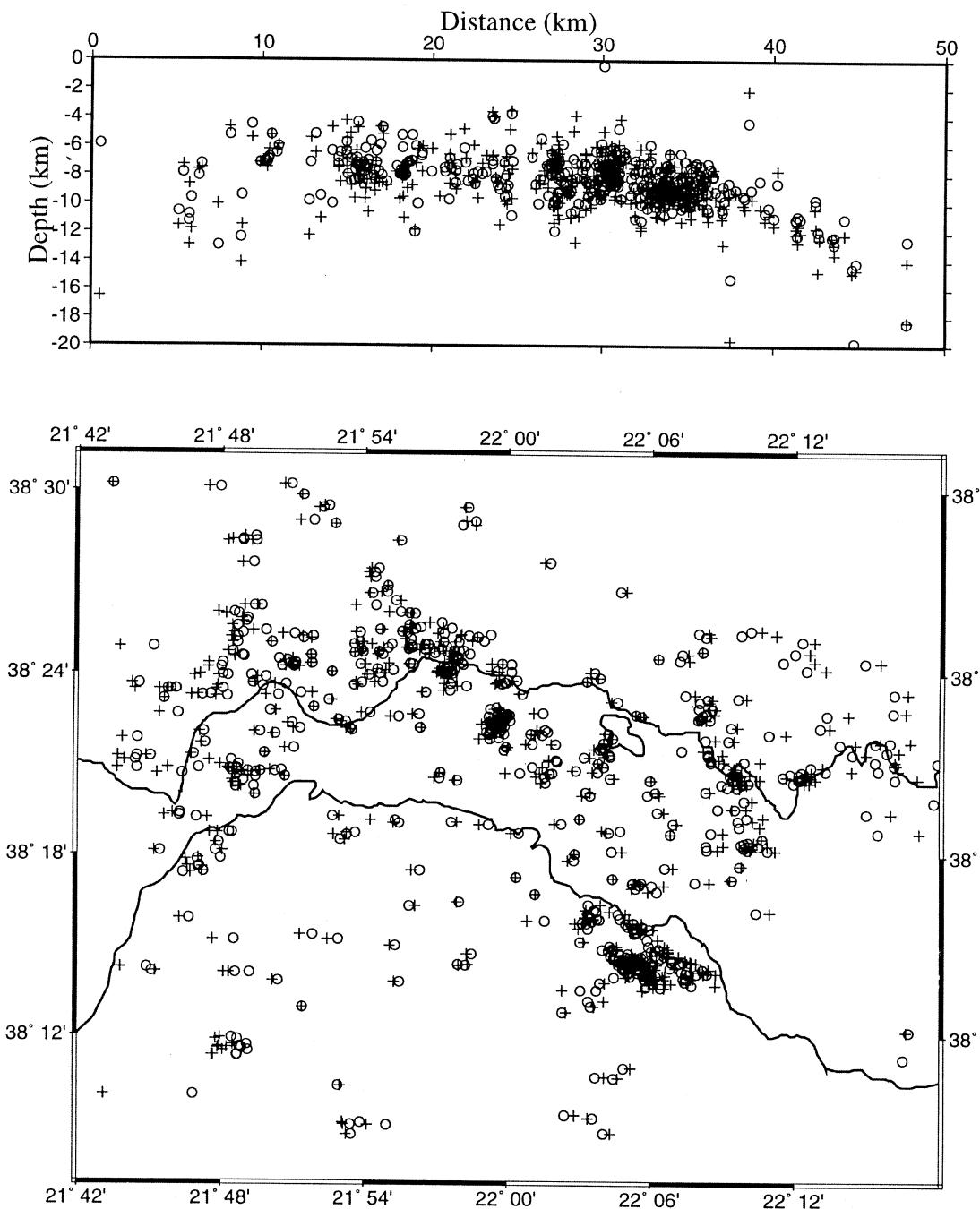


Fig. 12. Microevent relocation after the joint inversion for a 6 km grid: empty circles are initial positions while crosses are final positions.

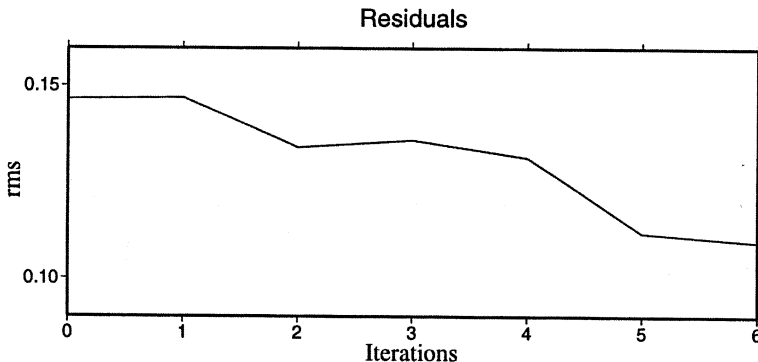


Fig. 13. The evolution of the misfit function with iteration. Note the two-step decrease illustrating the non-linearity of the procedure.

function remained almost unchanged. For example, at the KOUT station which is representative of the north-western part of the network, the r.m.s. decreased from 0.12 s to 0.03 s. Results (fig. 9b) at stations located on the southern coast, like the ANOZ station, show that initially important positive travel-time residuals were correctly explained by the presence of a low velocity anomaly. However, residuals at other stations such as the VELV station (fig. 9b) on the western limit of the network do not display a noticeable reduction. We believe this is possibly due to local effects. These particular residuals are responsible for the remaining high value of the global misfit function.

In our inversion method, we did not invert for station correction parameters. Their introduction would reduce the superficial anomalies observed in our present inversion and possibly help in fitting the data at stations such as VELV. We leave this task for future work.

7.6. Wavefront approach inversion

Despite the fact that the wavefront approach is expected to be less efficient than the ray approach for tomographic applications, we would like to investigate whether its ability to provide the global extremal ray connecting the source and the station has an important effect on this inversion. Moreover, we would like to see the

effect of formulating the inversion in terms of recovering the slowness field instead of the squared slowness, with a linear interpolation instead of a B-spline interpolation. In this application, the selected grid for the inversion had the same spacing as before. The finite difference estimation of first-arrival times was performed on a 100 by 100 by 100 grid related by linear interpolation to the inversion grid. On such grid, arrival times are computed with an accuracy better than 0.005 s. On that rather important grid, computing the ray from the source back to the receiver through wavefronts required for the inversion, is the most time-consuming part of the forward problem.

We performed only two iterations using this procedure and the P and S velocity structures (fig. 14a,b) display similar features to the ones obtained with the ray tracing approach: a low velocity anomaly along the southern shore line from the surface to 3 km depth and a transition to high velocity values directly under the network at 6–9 km depth. Down to 6 km, the agreement between the two approaches is good for both P and S velocities. The images are less stable at greater depths, illustrating the less constrained character of the structure.

The basic form of the velocity anomalies is confirmed by using different parameterizations of the model space, different interpolations over the inversion grid providing partial derivatives and different forward problem

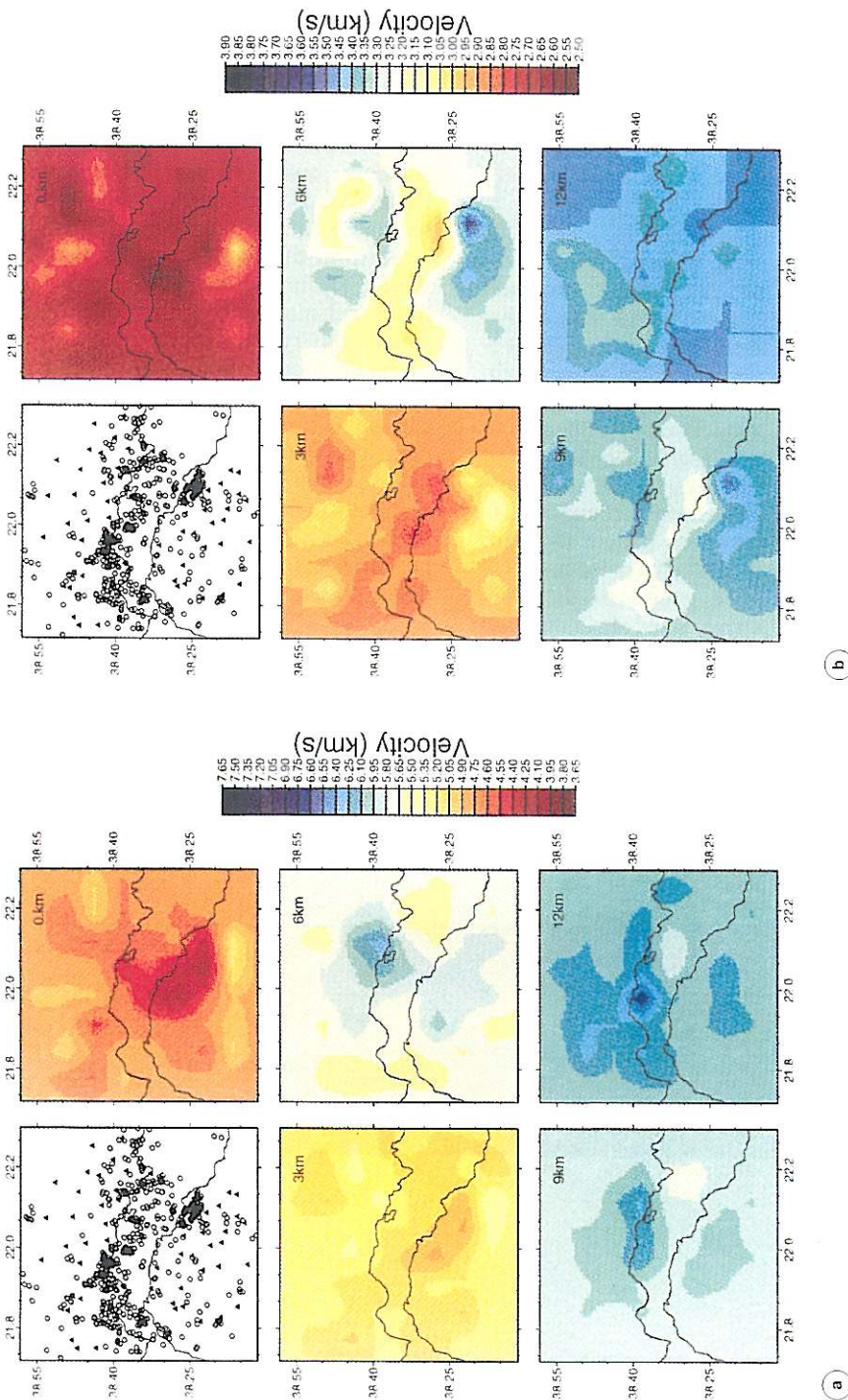


Fig. 14a,b. The 3D P (a) and S (b) velocity models after the joint inversion using waveform tracing for a 6 km grid.

solvers. The wavefront approach might be considered useful in the first iteration where the shooting angles of rays can be found and then used by the ray approach for further iterations.

7.7. Tectonic interpretation

This tomographic 3D velocity model provides new insights into the tectonic evolution of the Corinth gulf. The geological map of that area (fig. 8a) taken from the global seismotectonic map of Rigo shows evidence of two main tectonic episodes. The tertiary E-W compressive phase led to a subduction regime and to an high number of thrust faults. The associated Hellenic structures (fold axes and thrusts) have a N-S orientation in the eastern part and a NW-SE orientation in the western part of the gulf. The second phase is the post-miocene N-S extensional phase which generated the E-W system of current active normal faults and grabens. The asymmetry of the geological structure is clearly expressed by the extensive

plio-quaternary sedimentary deposits on the southern side of the gulf which are missing on the northern side. The sediments on the southern side are related to the infilling of grabens as normal faults displace and rotate the crust. The most active faults are those bordering the southern coast of the gulf, such as the Psathopyrgos fault and the Aigion fault. Older sediments on the southern side of the gulf derived from the former activity of southeastern normal faults subsequently have been uplifted, tilted and modified by the more recent extensional activity.

In all of our tomographic models, the velocity anomalies from the surface to 9 km depth can be related to the tectonic history of the area. The shallow structure in the south and inside the gulf shows a low velocity zone well correlated with the sedimentary deposits. The highest amplitude of the low velocity anomaly is found parallel to the graben structure at depths above 3 km depth where it is associated with sedimentary basins developed by the normal fault activity. As in other studies using local seismic tomography (Eberhart-Phillips and

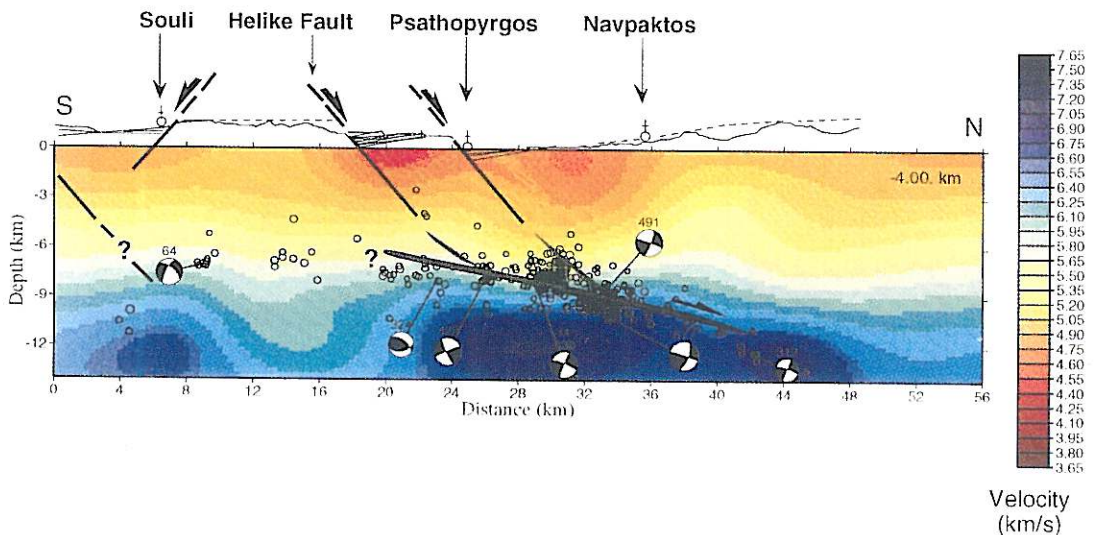


Fig. 15. Superposition of the recovered velocity model and a seismo-tectonic interpretation along the vertical cross-section AA' indicated in fig. 8b.

Michael, 1993; Scott *et al.*, 1994), we found that shallow structures are spatially correlated with the fault zone geology. At greater depth, the amplitude of the low velocity anomaly decreases and moves to the North, in agreement with the dip of faults observed at the surface. A vertical section (fig. 15) in the western part of the P velocity structure (from A to A' in fig. 8b) shows the depth extent of the anomalies associated with the surface geology.

The layer between 6 km and 9 km seems to correspond to a transition zone where the velocity distribution is no longer correlated with surface fault traces. The low velocity anomaly visible at 3 km depth disappears and a high velocity anomaly appears under the central part of the network at a depth of 9 km.

This transition zone might correspond to the mechanical transition zones between brittle and ductile behaviour of the crust. Evidence of similar velocity structure was obtained in local tomographic studies of the crust in California (Eberhart-Phillips and Michael, 1993; Foxall *et al.*, 1993; Scott *et al.*, 1994). In these studies, the abrupt change from the shallow velocity structure which is correlated with surface fault features to an uncorrelated velocity structure occurs in the 9–12 km depth range. For the Corinth gulf, this transition zone is shallower at around 6–9 km depth. This may indicate a shallower brittle/ductile transition than in California possibly due to increased heat flow below this very active extensional regime. This brittle/ductile mechanical transition zone may be the site of strain concentration which can produce large stresses important for the generation of the observed seismicity. We speculate that this depth could be the nucleation depth for the rupture of a significant earthquake in this area.

8. Conclusions

In our tomographic analysis, we have used two different forward modeling techniques to produce a robust image of the crust in the Gulf of Corinth. We illustrated the influences of parameterization and interpolation over finite grids. The ray method is a fast approach once initial angles for each source/station pair are

roughly estimated. We think a wise strategy for seismic tomography is to handle this estimation of initial angles apart from the tomographic kernel. Wavefront approaches, that is ray tracing based on graph theory or any other global sampling of the 3D medium, are powerful methods to deduce these angles. Once they are obtained, one might proceed with the ray approach using linearized inversion retaining the initial angles through subsequent iterations. We found that the local misfit function at each station gives a better picture of the inversion performance than the global misfit function. Finally we found that the normalization between parameters is a key controlling the quality of the recovered image. Only synthetic tests were able to provide values of the different weightings between parameters for a given station and earthquake distribution.

In addition to these methodological points, the application to the tectonically active Patras area demonstrates the power of this 3D seismic tomography approach to constrain variations in velocity inside the crust. This is particularly important at seismogenic depths where the mapping of the subsurface cannot be extrapolated. In spite of the lack of stations inside the gulf, we were able to recover a low velocity feature associated with the half-graben tectonic structure. The sharp increase in velocity at 6–9 km depth could correspond to a tectonic discontinuity as suggested by Rigo (1994) or a change in material competence. Moreover, we might claim, as in other recent crustal tomographic study zones, that a possible correlation exists between an increase in seismic velocity and an increase in the ability to store strain energy and release it as brittle failure.

Acknowledgements

We acknowledge the partial support of the Institut National des Sciences de l'Univers through the *Tomographie* program. We thank H. Lyon-Caen and all the colleagues who have contributed to the Patras experiment for the data acquisition and processing and helpful discussions. We are deeply indebted to Jennifer Haase for a critical review of the manuscript.

REFERENCES

- AKI, K. and W. LEE (1976): Determination of three-dimensional velocity anomalies under a seismic array using first P -arrival times from local earthquakes. 1. A homogeneous initial model, *J. Geophys. Res.*, **81**, 4381-4399.
- AL-SHKURI, H. and B. MITCHELL (1988): Reduced seismic velocities in the source zone of New Madrid earthquakes, *Bull. Seism. Soc. Am.*, **78**, 1491-1509.
- BILLIRIS, H., D. PARADISSIS, G. VEIS, P. ENGLAND, W. FEATHERSTONE, B. PARSONS, P. CROSS, P. RANDS, M. RAYSON, P. SELLERS, V. ASHKENAZI, M. DAVISON, J. JACKSON and N. AMBRASEYS (1991): Geodetic determination of tectonic deformation in Central Greece from 1900 to 1988, *Nature*, **350**, 124-129.
- BREGMAN, N., R. BAILEY and C. CHAPMAN (1989): Cross-hole seismic tomography, *Geophysics*, **54**, 200-215.
- BRIOLE, P., J. RUEGG, H. LYON-CÄEN, A. RIGO, K. PAZISSI, G. VEIS, D. HATZFELD and A. DESCHAMPS (1994): Active deformation of the Gulf of Corinth, Greece: results from repeated GPS surveys between 1990 and 1993, *Ann. Geophys.*, **12** (suppl. 1), C65.
- BURRIDGE, R. (1976): *Some Mathematical Topics in Seismology* (Courant Institute of Mathematical Sciences, New York University).
- CROSSON, R. (1976a): Crustal structure modeling of earthquake data. 1. Simultaneous least squares estimation of hypocenter and velocity parameters, *J. Geophys. Res.*, **81**, 3036-3046.
- CROSSON, R. (1976b): Crustal structure modeling of earthquake data. 2. Simultaneous least squares estimation of hypocenter and velocity parameters, *J. Geophys. Res.*, **81**, 3047-3054.
- DINES, K. and J. LYTHE (1979): Computerized geophysical tomography, *Proc. IEEE*, **67**, 1065-1073.
- EBERHART-PHILLIPS, D. and A. MICHAEL (1993): Three-dimensional crustal velocity structure in the Parkfield, California, region from inversion of local earthquake and shot arrival times, *J. Geophys. Res.*, **99**, 15737-15758.
- FARRA, V. and R. MADARIAGA (1987): Seismic waveform modeling in heterogeneous media by ray perturbation theory, *J. Geophys. Res.*, **92**, 2697-2712.
- FARRA, V., J. VIRIEUX and R. MADARIAGA (1989): Ray perturbation theory for interfaces, *Geophys. J. Int.*, **99**, 377-390.
- FOXALL, W., A. MICHELINI and T. MCEVILY (1993): Earthquake travel-time tomography of the Southern Santa Cruz mountains: control of fault rupture by lithological heterogeneity of the San Andreas fault zone, *J. Geophys. Res.*, **98**, 17691-17710.
- IVANSSON, S. (1983): Remark on an earlier proposed iterative tomographic algorithm, *Geophys. J. R. Astron. Soc.*, **75**, 855-860.
- JULIAN, B. and D. GUBBINS (1977): Three dimensional seismic ray tracing, *J. Geophys.*, **43**, 95-114.
- KELLER, H. and P. PEROZZI (1983): Fast seismic ray tracing, *SIAM J. Appl. Math.*, **43**, 981-992.
- KISSLING, E., W. ELLSWORTH, D. EBERHART-PHILLIPS and U. KRADOLFER (1994): Initial reference models in local earthquake tomography, *J. Geophys. Res.*, **99**, 19635-19646.
- LEE, W. and J. LAHR (1975): HYPO71: a computer program for determining hypocenter, magnitude, and first motion pattern of local earthquakes, *Open-file report, USGS*, **75**, 311.
- LÉVÉQUE, J., L. RIVERA and G. WITTLINGER (1993): On the use of the checker-board test to assess the resolution of tomographic inversions, *Geophys. J. Int.*, **115**, 313-318.
- MENKE, W. (1984): *Geophysical Data Analysis: Discrete Inverse Theory* (International Series, Academic Press, San Diego CA).
- NOLET, G. (1981): Linearized inversion of (teleseismic) data, in *The Solution of the Inverse Problem in Geophysical Interpretation*, edited by R. CASSINIS (Plenum, New York), 9-37.
- NOLET, G. (1985): Solving or resolving inadequate and noisy tomographic systems, *J. Comp. Phys.*, **61**, 463-482.
- NOLET, G. (1987): Waveform tomography, in *Seismic Tomography*, edited by G. NOLET (Reidel, Dordrecht), 301-322.
- PAIGE, C. and M. SAUNDERS (1982): LSQR: an algorithm for sparse linear equations and sparse least squares, *ACM Trans. Math. Softw.*, **8**, 43-71.
- PODVIN, P. and I. LECOMTE (1991): Finite difference computation of travel-times in very contrasted velocity models: a massively parallel approach and its associated tools, *Geophys. J. Int.*, **105**, 271-284.
- RIGO, A. (1994): Étude seismotectonique et géodésique du Golfe de Corinthe (Grèce), *Thèse de l'Université Paris 7*.
- RIZNICHENKO, Y. (1946): Geometrical seismics of layered media, *Trudy Inst. Theor. Geophysics.*, **2**, Izo. AN SSSR, Moscow (in Russian).
- SAMBRIDGE, M. and B. KENNEDY (1986): A novel method of hypocenter location, *Geophys. J. R. Astron. Soc.*, **87**, 679-697.
- SCOTT, J., T. MASTERS and F. VERNON (1994): 3D velocity structure of the San Jacinto fault zone near Anza, California. 1. P waves, *Geophys. J. Int.*, **119**, 611-626.
- SPAKMAN, W. (1988): Upper mantle delay time tomography, *Ph.D. Thesis*, University Rijksuniversiteit, Utrecht.
- SPAKMAN, W. and G. NOLET (1988): Imaging algorithms, accuracy and resolution, in *Delay Time Tomography*, edited by N. VLAAR, G. NOLET, M. WORTEL, S. CLOETINGH and D. REIDEL, *Math. Geophys.*, 155-187.
- TARANTOLA, A. and B. VALETTE (1982): Generalized non-linear inverse problems solved using least squares criterion, *Rev. Geophys. Space Phys.*, **20**, 219-232.
- THURBER, C. (1983): Earthquake locations and three dimensional crustal structure in the Coyote Lake area, Central California, *J. Geophys. Res.*, **88**, 8226-8236.
- TRAMPERT, J. and J. LÉVÉQUE (1990): Simultaneous iterative reconstruction technique: physical interpretation based on the generalized least squares solution, *J. Geophys. Res.*, **95**, 12553-12559.
- VAN DER SLUIS, A. and H. VAN DE VORST (1987): Numerical-solution of large, sparse linear systems arising from tomographic problems, in *Seismic Tomography*, edited by G. NOLET (Reidel, Dordrecht), 53-57.
- VIDALE, J. (1988): Finite-difference calculation of travel times, *Bull. Seism. Soc. Am.*, **78**, 2062-2076.
- VIRIEUX, J., V. FARRA and R. MADARIAGA (1988): Ray tracing in laterally heterogeneous media for earthquake location, *J. Geophys. Res.*, **93**, 6585-6599.
- ZHAO, D., A. HASEGAWA and S. HORIUCHI (1992): P -wave tomographic imaging of the crust and upper mantle, *J. Geophys. Res.*, **97**, 19909-19928.